# Development of an Airborne-Based GPR System for Landmine and IED Detection: Antenna Analysis and Intercomparison

**MARÍA GARCÍA FERNÁNDEZ**[1], **GUILLERMO ÁLVAREZ NARCIANDI**[1],
**ANA ARBOLEYA**[2], **(Member, IEEE), CARLOS VÁZQUEZ ANTUÑA**[1],
**FERNANDO LAS-HERAS ANDRÉS**[1], **(Senior Member, IEEE),**
**AND YURI ÁLVAREZ LÓPEZ**[1]

[1]Área de Teoría de la Señal y Comunicaciones, Departamento de Ingeniería Eléctrica, Universidad de Oviedo, 33203 Gijón, Asturias, Spain
[2]Área de Teoría de la Señal y Comunicaciones, Departamento de Teoría de la Señal y las Comunicaciones y Sistemas Telemáticos y Comutación, Universidad Rey Juan Carlos, 28943 Fuenlabrada, Madrid, Spain

Corresponding author: Yuri Álvarez López (alvarezyuri@uniovi.es)

**ABSTRACT** Airborne-based Ground Penetrating Radar (GPR) systems have proved to be an efficient solution for safe and accurate detection of buried threats such as Improvised Explosive Devices (IEDs) and anti-personnel and anti-tank landmines. The design of these prototypes is influenced by several parameters such as the working frequency band or the maximum weight and size of the payload to be placed on board the Unmanned Aerial Vehicle (UAV). In this sense, one of the main bottlenecks found in the design of these systems is the proper selection of the GPR antenna. This contribution focuses on the analysis of different Ultra Wideband (UWB) Vivaldi antennas and their performance in the context of an airborne-based GPR system. First, the Vivaldi antennas are characterized in terms of $S_{11}$, radiation pattern, directivity, and phase center. Next, they are placed on board the implemented airborne-based GPR prototype to assess their impact on the detection capabilities of the system. In addition, other criteria such as the weight and size of the antennas are considered to make the final selection. Finally, the selected UWB Vivaldi antennas are tested in a realistic scenario.

**INDEX TERMS** Ground Penetrating Radar (GPR), Ultra Wideband (UWB) antenna, Vivaldi antenna, unmanned aerial vehicle (UAV), Synthetic Aperture Radar (SAR), antenna measurement.

## I. INTRODUCTION

The development of systems for secure and fast detection of landmines, Improvised Explosive Devices (IEDs) and UneXploded Ordnances (UXOs) is a technological challenge that has been addressed using different approaches, such as handheld detectors [1], [2], autonomous robots [3], [4], vehicle-mounted detection systems [5] and, in recent years, Unmanned Aerial Vehicles (UAVs). The latter are of special interest from the safety point of view, as they enable

The associate editor coordinating the review of this manuscript and approving it for publication was Chinmoy Saha.

contactless detection capabilities. Besides, they are able to operate in difficult-to-access scenarios.

Different types of sensors can be integrated within UAVs for landmine and IED detection. In this regard, metal detectors [6] and magnetometers [7] are limited to the detection of metallic targets. In contrast, Ground Penetrating Radar (GPR) sensors are capable of finding either metallic or non-metallic targets, provided they have enough dielectric contrast with the medium in which they are buried.

Airborne-based GPR systems can resort to different architectures. For example, a side-looking GPR is presented in [8], whereas [9]–[12] propose a Down-Looking GPR

architecture. Thanks to the improvements in positioning subsystems (e.g. Global Navigation Satellite System - Real Time Kinematics, GNSS-RTK), GPR measurements can be georeferred with centimeter-level accuracy, enabling Synthetic Aperture Radar (SAR) processing. Consequently, cross-range or lateral resolution of GPR images is improved, yielding better detection capabilities. [8] proposes a Circular-based Synthetic Aperture Radar (CSAR), in which the UAV flies in circles around the area to be scanned, whilst in [12], SAR processing uses the down-looking area scanned by the UAV (i.e. DL-GPR SAR). A summary of the most recent prototypes developed for landmine and IED detection using UAVs is presented in Table 1 of [12], where it can be noticed that most of them operate in the L and S bands (1 to 4 GHz). This frequency range constitutes a good trade-off between image resolution (around 5-7 cm free-space range resolution) and penetration depth.

One of the key issues in the design of an airborne-based GPR system is the choice of the GPR antennas. It is well known that the larger the bandwidth, the better the range resolution. Besides, the frequency must be kept low enough to avoid high penetration losses. Thus, the use of Ultra Wideband (UWB) antennas and radar modules is required. However, the radiofrequency characteristics of the antennas are not the only aspect to take into account. As the antennas will be included in the UAV payload, special attention must be paid to their mechanical specifications (weight, size and shape). For example, in [10] two 240 g weight and 9.5 cm × 22.5 cm × 18 cm size Vivaldi-horn antennas, operating within the 550-4000 MHz frequency band, are used. A similar antenna design is shown in [8]. In contrast, the proposed airborne-GPR prototypes of [11], [12] incorporate planar antennas.

Although the Vivaldi-horn antennas used in [8], [10] seem to offer better radiofrequency characteristics, exhibiting low dispersion (which means that the antenna phase center barely changes with frequency), their relative bulkiness can jeopardize the UAV stability (especially in windy conditions, regardless of wind direction). In contrast, planar antennas such as the ones shown in [11], [12], which occupy a smaller volume, make the integration in the UAV easier.

Cavity-backed antennas such as helix [13] and sinuous [14] ones provide good performance in terms of bandwidth and directivity, making them suitable for GPR applications. However, the considerable weight of the resonant cavity, which can exceed 1 kg, limits its use in airborne-based GPR systems.

This contribution is focused on the analysis of different types of UWB Vivaldi antennas for the implementation of the UAV prototype described in [12], including both commercial and custom-designed Vivaldi antennas. Apart from an accurate characterization of antenna radiation parameters at spherical range in anechoic chamber, the novelty of this contribution is the benchmarking of candidate Vivaldi antennas on board the airborne-based GPR systems. Thus, the performance of these Vivaldi antennas concerning detection

capabilities is directly tested in realistic scenarios using the UAV prototype. A video summarizing the contents of this contribution is available at https://youtu.be/2xAZIZnkL1M.

## II. ANTENNA SELECTION/DESIGN AND CHARACTERIZATION

The airborne GPR-based system, presented in [12], is based on a commercial airframe [15] with a maximum take-off weight of 11 kg. The GPR subsystem is based on an UWB radar module operating from 100 MHz to 6 GHz [16]. This module has one transmitting port and two receiving ports. Thus, to take advantage of the full capability of the radar module, it is desirable to integrate three antennas on board the UAV following a receiving-transmitting-receiving arrangement (Rx-Tx-Rx), as described in [12].

### A. SELECTION OF THE GPR ANTENNAS

Concerning the choice of the antennas for the GPR subsystem, the following requirements have been initially defined: i) working frequency band: approximately from 900 MHz to 3000 MHz; ii) overall weight < 700 g (as three antennas are used, that is < 233.3 g per antenna); iii) size: planar antennas preferred (if possible, not larger than 30 cm × 25 cm). The antenna bandwidth is defined according to the $S_{11} < -7$ dB criterion, which for this targeted application (airborne-based GPR) has been found to be acceptable. Nevertheless, this characteristic is not sufficient to assess the performance of the tested GPR antennas. Therefore, a more complete antenna characterization and benchmarking is presented in this contribution. The highest frequency is limited to 3000 MHz because in most of the GPR scenarios frequencies above 3 GHz exhibit poor penetration into the ground.

According to the previous requirements, three commercial UWB Vivaldi antenna models have been considered: TSA 600 Vivaldi antenna [17] (hereinafter referred to as *large Vivaldi*), TC930-83 [18] (referred to as *dual polarized Vivaldi*), and IS-AV-0106G [19] (referred to as *small Vivaldi*). Some of their specifications are listed in Table 1. It must be pointed out that the *large Vivaldi* [17] has been already considered in previous airborne-based GPR system prototypes, finding that it exhibited a low dispersive frequency response despite its size. Thus, one of the goals of the research presented in this contribution is to compare the performance of this antenna with other potential candidates for UAV integration.

### B. CUSTOMIZED ANTENNA DESIGN

In addition to the three commercial antennas chosen for the comparison, the design of a *customized Vivaldi* antenna has been proposed, aiming at minimizing size and weight while keeping acceptable bandwidth and radiation parameters. The antenna was designed in 1.6 mm thick FR4 substrate ($\varepsilon_r = 4.3$, tan $\delta = 0.019$), with a copper thickness of 35 $\mu$m. Later, the custom-designed Vivaldi antenna was manufactured in house using LPKF H100 prototyping equipment [20].

**TABLE 1.** Specifications of the UWB Vivaldi antennas to be compared. In the case of commercial antennas, specifications correspond to the values given in the antenna datasheet.

| Antenna model | Bandwidth (MHz) | Dimensions (cm) | Weight (g) | Polari-zation |
|---|---|---|---|---|
| TSA 600 [17] (*large Vivaldi*) Fig. 1 (a) | 600-6000 | 24 width 33 length | 230 | Linear |
| TC930-83 [18] (*dual pol. Vivaldi*) Fig. 1 (b) | 600-8000 | 13 × 13 × 7 | 37 | Dual pol. |
| IS-AV-0106G [19] (*small Vivaldi*) Fig. 1 (d) | 1000-6000 | 10 width 16 length | 100 | Linear |
| Customized design (*customized Vivaldi*) large prototype Fig. 1 (c), central ant. | 500-3000 | 22 width 22 length | 150 | Linear |
| Customized design (*customized Vivaldi*) small prototype Fig. 1 (c), side ant. | 500-3000 | 20 width 20 length | 130 | Linear |



**FIGURE 1.** Antennas selected for the study (pictures not to scale), assembled following a Rx-Tx-Rx arrangement (as in the UAV). (a) TSA 600 antenna [17] (*large Vivaldi*). (b) Dual-polarized TC-93083 antenna [18] (*dual-polarized Vivaldi*). (c) *Customized Vivaldi* antenna design. (d) Vivaldi antenna IS-AV-0106G [19] (*small Vivaldi*).

The antenna is a standard Vivaldi design with a wideband microstrip to slot transition. The transition was implemented as defined in [21], by means of a lambda quarter transformer in order to match the 50 Ω of the connector to the impedance of the slot, and two lambda quarter radial stubs in the slot and microstrip ends to simulate a virtual short circuit at the connection point between both structures. The radial stub of the slotline was replaced by a circular cavity that exhibited better performance across the entire band.

Antenna size minimization was achieved by means of a set of non-symmetrical rectangular corrugations etched on the non-radiating edges of the antenna, following the guidelines given in [22], [23]. The etched corrugations behave as a high impedance structure for the surface waves which are suppressed along the non-radiating edges, increasing the current flow along the exponential tapered slot. In this way, the operational bandwidth can be extended towards the lower frequencies while maintaining the size of the antenna. The rectangular corrugations also contribute to improve the radiation parameters and antenna gain [23].

A first antenna prototype of size 22 cm × 22 cm was manufactured (see Fig. 2, right). A second prototype was also manufactured, based on a refined design aimed at reducing the size of the antenna and improving its directivity. The size of the second prototype was 20 cm × 20 cm (see Fig. 2, left). The weight of the *customized Vivaldi* antenna prototypes are 130 g for the small prototype and 150 g for the large prototype.

With regard to the integration within the UAV, the first prototype is used as transmitting antenna, with one unit of the second prototype placed at either side for the reception, as shown in Fig. 1 (c).
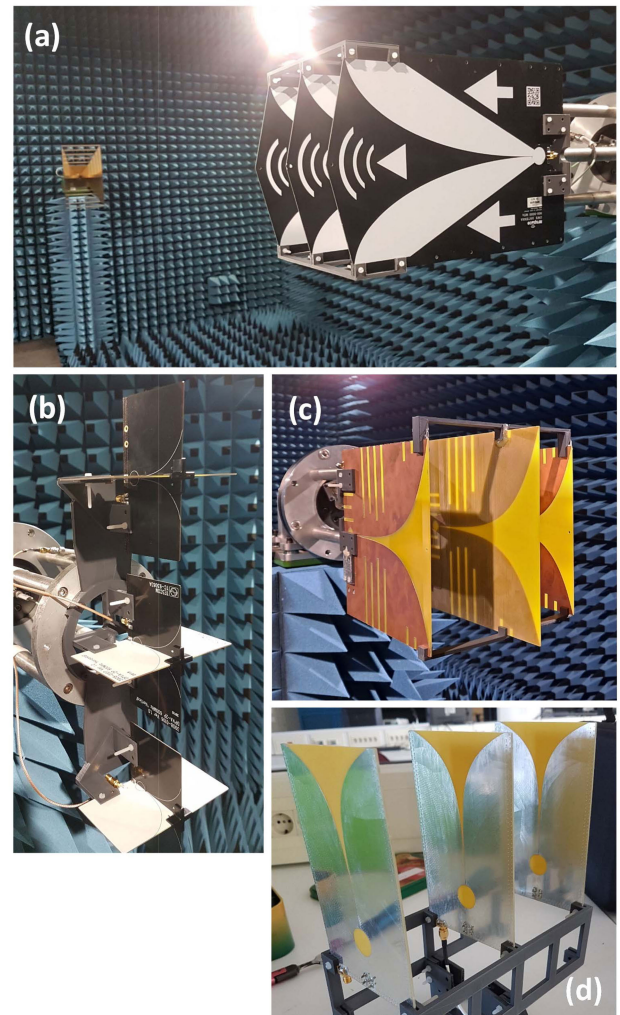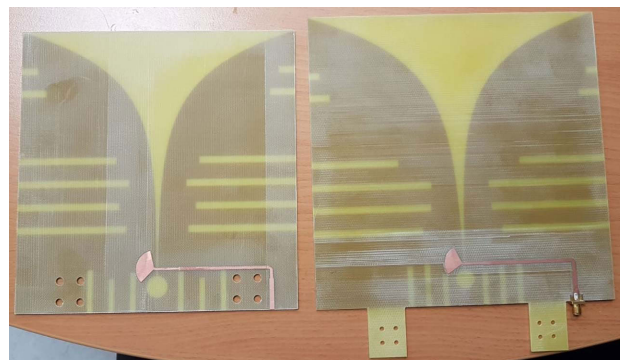


**FIGURE 2.** Picture of the manufactured prototypes of the *customized Vivaldi* antenna. Right: first (large) prototype. Left: second (small) prototype.

## C. ANTENNA CHARACTERIZATION

Antennas were characterized using the same arrangement to be placed on board the UAV, that is, placing the three
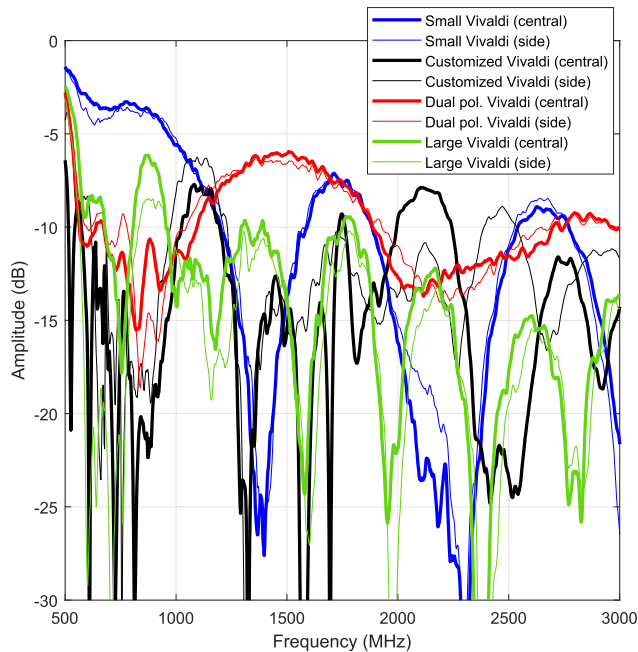
**FIGURE 3.** Measured $S_{11}$ parameter of the analyzed antennas.

antennas (the two side antennas for the receiving channels of the radar module and the central one for the transmitter) on the structure to be attached to the airframe. The goal was to assess the impact of effects such as mutual coupling in the radiation performance. Spacing between antennas is 9.8 cm except in the case of the *dual polarized Vivaldi* [18] that had to be increased to 15 cm to fit the three antennas using the space at the UAV platform.

In terms of wavelength (λ), the 9.8 cm spacing corresponds to 0.2λ and 1λ at 600 MHz and 3 GHz, respectively. For the *dual polarized Vivaldi*, the 15 cm spacing corresponds to 0.3λ at 600 MHz, and 1.5λ at 3 GHz. Note that, as indicated in [12], the GPR-SAR images obtained from the measurements collected with each receiving antenna are combined to improve signal-to-clutter ratio, taking advantage of receiving channel redundancy.

First, the $S_{11}$ parameter was measured. As observed in Fig. 3, the $S_{11}$ of all the UWB Vivaldi antennas is lower than −7 dB from approximately 600 MHz up to 3000 MHz, except from 1300 MHz to 1700 MHz in the case of the *dual polarized Vivaldi* antenna, and below 1100 MHz for the *small Vivaldi* antenna. The central antenna of the *large Vivaldi* and the side antenna of the *customized Vivaldi* also exhibit a $S_{11}$ slightly above −7 dB around 800 MHz and 1100 MHz, respectively.

Concerning the impact of mounting the antennas according to the Rx-Tx-Rx arrangement, it can be noticed that, overall, the $S_{11}$ parameter of the central antenna is slightly worse than the $S_{11}$ of the side antennas, although these differences are less than 2-3 dB. Nonetheless, this still has some impact, especially when the $S_{11}$ is close to −7 dB, as is the case of the *large Vivaldi* around 800 MHz. Only in the case of the *customized Vivaldi* antennas, the $S_{11}$ of the central and side antennas exhibit significant differences above 2 GHz, due

to the fact that, as explained in Section II-B, two different prototypes of the *customized Vivaldi* were manufactured: the central antenna is slightly larger than the side antennas (see Fig. 2).

Next, the antenna radiation pattern was measured at the spherical range in the anechoic chamber of the University of Oviedo. Measurements were conducted from 600 MHz up to 3000 MHz, in 30 MHz-steps.

Antennas were characterized alone as well as mounted according to the aforementioned Rx-Tx-Rx arrangement (as shown in Fig. 1), measuring both central and side antennas. To illustrate this, Fig. 4 shows a comparison of the E-plane cuts of the radiation pattern for the *large Vivaldi* when measured alone and in the Rx-Tx-Rx arrangement. It can be noticed that the radiation pattern of the central antenna is partially distorted, especially at lower frequencies ($f = 1$ GHz). For higher frequencies, the Rx-Tx-Rx arrangement does not produce significant degradation of the radiation pattern (differences are less than 3-4 dB in the main lobe). The other three compared antennas exhibit a similar behavior (radiation parameters of the central antenna are worse than those of the side ones).

Antenna directivity is plotted in Fig. 5. In general, as the electric size of the AUT increases with frequency, it can be expected that the directivity increases as well within the working frequency band of the AUT. The *large Vivaldi* antenna exhibits the highest directivity, which is related to the fact that it also has the largest electric size. This is also observed in the case of the *customized Vivaldis*, where the larger prototype is, in general, more directive than the smaller ones. Concerning the *small Vivaldi* antenna, its directivity is the lowest below 1500 MHz, and above this frequency it follows a behavior similar to the *dual-polarized Vivaldi* antenna. From the results shown in Fig. 5, it can be concluded that the directivity of the central antenna is, in general, smaller than that of the side antennas.

Fig. 6 shows the E-plane of the compared antennas (for the sake of simplicity, only the central antenna is shown, as it corresponds to the worst-case scenario), whereas the boresight level within the analyzed frequency band is depicted in Fig. 7. The boresight level corresponds to the amplitude of the field level measured with the Vector Network Analyzer of the anechoic chamber when the AUT and the probe antenna are pointing to each other. The boresight level depends mainly on the free-space propagation losses and the attenuation of cables and connectors, which increase with frequency, and the directivities of the AUT and the probe. Thus, if the increase of the directivity with frequency is smaller than the increase of free-space propagation losses and the attenuation introduced by cables and connectors, the boresight level decreases with frequency, as observed in Fig. 7.

Up to 1200 MHz, the *large, customized and dual-polarized Vivaldi* antennas exhibit similar boresight levels. Above 1500 MHz, the boresight level of the *dual-polarized Vivaldi* decreases sharply (around 5-6 dB), and its main beam broadens (Fig. 6, 2 GHz and 3 GHz). A similar behavior is noticed
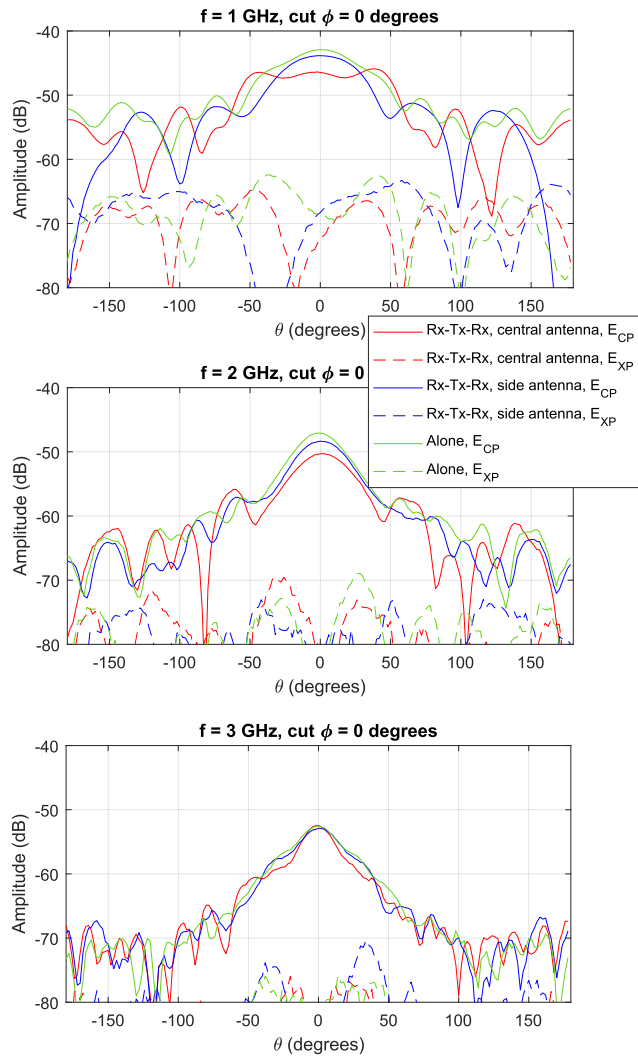
**FIGURE 4.** Comparison of the radiation pattern of the *large Vivaldi* antenna [17] measured alone as well as in a Rx-Tx-Rx arrangement. E-plane ($\phi = 0°$) cut. $E_{CP}$: co-polar component. $E_{XP}$: cross-polar component.



**FIGURE 5.** Comparison of the directivity of the analyzed Vivaldi antennas.

around 2 GHz in the case of the *customized Vivaldi* antennas. The *large Vivaldi* antennas (either the central or the side ones) present a steady decrease of the boresight level with frequency (a decay of 4.2 dB/GHz approximately). In the case of the *small Vivaldi*, the boresight level is the lowest below 1500 MHz. The largest co-polar to cross-polar ratio corresponds to the *large Vivaldi*, being greater than 20 dB from 1 GHz to 3 GHz.

It must be remarked that the variation of the amplitude in the frequency response of the antennas (Fig. 7) can be equalized in the GPR-SAR processing [24], by means of the normalization of the GPR-SAR images recovered for each discrete frequency, then combining all these GPR-SAR images coherently. Thanks to this, contributions of each discrete frequency will have the same weight in the resulting GPR-SAR image. In any case, the lower the boresight level, the weaker the field scattered by buried targets.
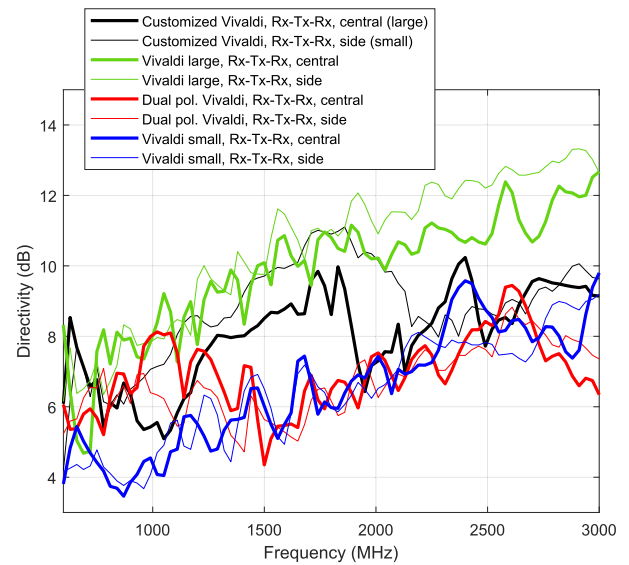
Antenna dispersion is another important parameter in the framework of GPR systems, as dispersive antennas might degrade the frequency response of the whole GPR system. In this sense, minimizing antenna dispersion while keeping antenna directivity high in the working frequency band was one of the design goals of the Vivaldi-horn antenna presented in [10]. Antenna dispersion and its relationship with the antenna phase center was also studied in [25], where a Vivaldi, a log-periodic, and a monopole antenna were compared.

The methodology followed for obtaining the phase center is the widely used least squares fit method described in Section IV.A of [26]. It consists of comparing, for each discrete frequency within the working frequency band, the measured phase of the AUT and the theoretical one calculated for different distances. The distance that gives the smallest deviation between the theoretical and the measured phase is taken as the phase center position.

Fig. 8 shows the variation of the phase center of the analyzed Vivaldi antennas with frequency. The phase center of the *large Vivaldi* antenna is quite stable above 1200 MHz (especially if compared to its electric size), with smaller displacements than the *dual-polarized Vivaldi* and *customized Vivaldi* antennas. The latter exhibits large phase center displacements at those frequencies where the boresight level has a sharp decrease. The *small Vivaldi* antenna has significant displacements (up to 25 cm) below 1500 MHz.

Finally, it must be mentioned that, apart from the Vivaldi antennas listed in Table 1, all of them having linear polarization, spiral antennas with circular polarization working in the 650 MHz - 3000 MHz frequency band were also tested. However, they exhibited quite a dispersive response due to the large displacement of the antenna phase center in the aperture plane of the spiral antenna, which introduced even more dispersion in the GPR-SAR images than linearly polarized
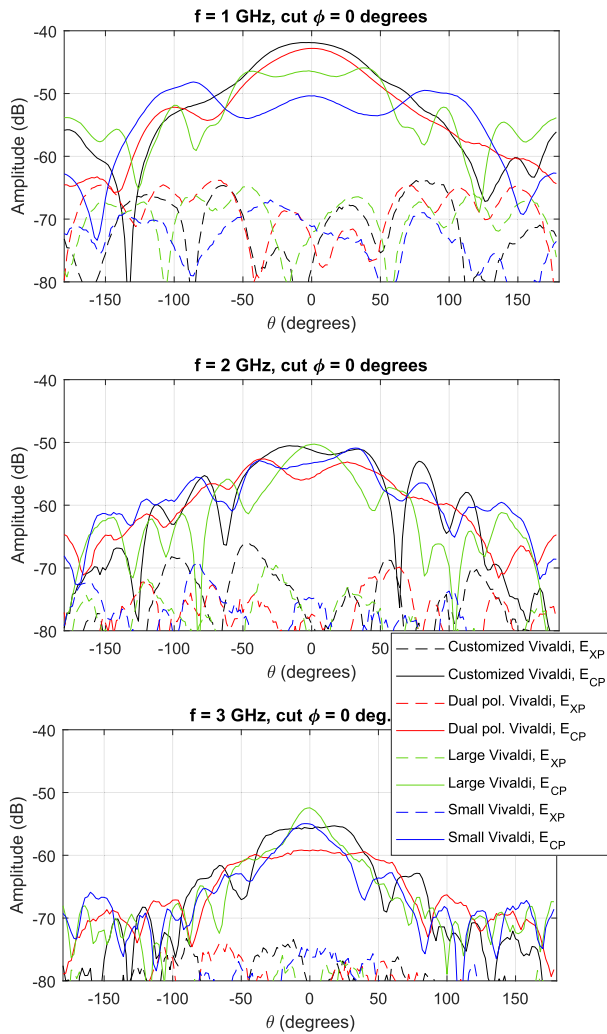
**FIGURE 6.** Comparison of the E-plane radiation pattern of the Vivaldi antennas. E-plane ($\phi = 0°$) cut. $E_{CP}$: co-polar component. $E_{XP}$: cross-polar component.



**FIGURE 7.** Comparison of the boresight level of the analyzed Vivaldi antennas. $E_{CP}$: co-polar component. $E_{XP}$: cross-polar component.
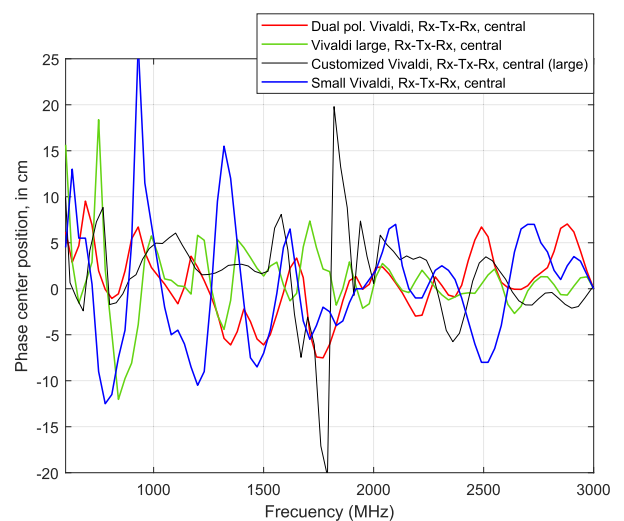


**FIGURE 8.** Phase center of the compared Vivaldi antennas vs. frequency. For comparison purposes, a reference phase of 0 degrees is taken at 3 GHz.

antennas, where the antenna phase center shifts along the axis containing the antenna main beam (Fig. 8).

## III. ANALYSIS OF GPR CAPABILITIES

### A. FIRST VALIDATION SCENARIO

The first validation scenario is located within the airfield of the University of Oviedo, Gijón, Spain. For a fairer comparison of the selected antennas, flights were performed over the same area of 1.5 m width × 6 m length, where the grass had been previously removed and the targets had been buried. Measurements were conducted on the same day, within a two-hour interval. Soil moisture and weather conditions remained almost invariant during the tests. A relative permittivity ($\varepsilon_r$) ranging from 6 to 7 was estimated from GPR-SAR measurements and the known depth of the detected targets.

The *large, customized,* and *small Vivaldi* antennas were placed on board the same UAV platform [15], keeping the same hardware and configuration parameters for all measure-
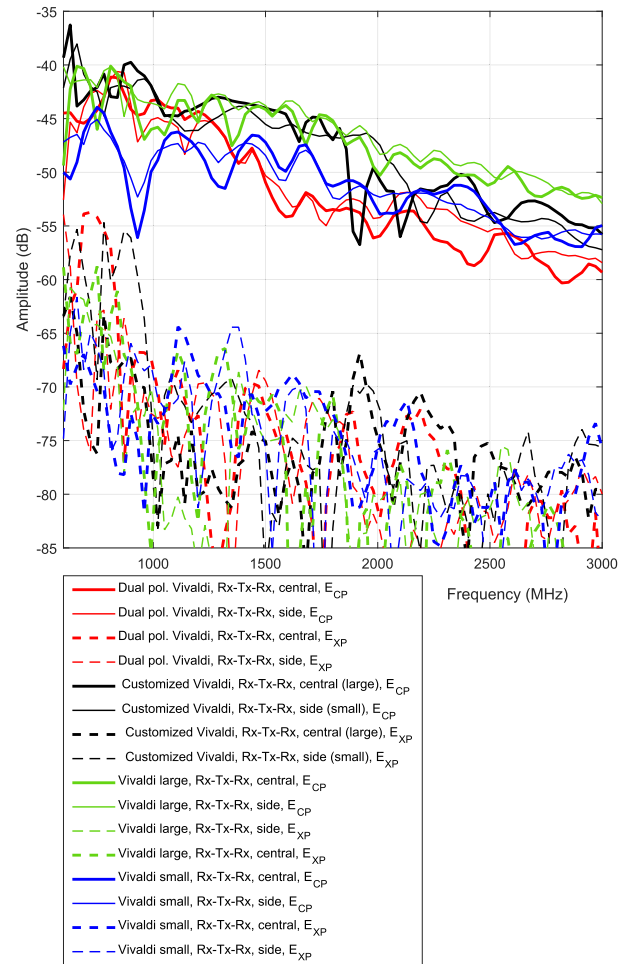
ments. *Dual-polarized Vivaldi* antennas were also tested on board the UAV in a previous measurement campaign, but the

**TABLE 2.** First validation scenario. Buried targets.

| Object | Size (cm) | Depth (cm) | Other specs. |
|---|---|---|---|
| First group of metallic plates | 10 × 10 (5 ×5 each) | 14 | 3 plates |
| Wooden trunk-like IED | 25 long × 15 ∅ Vert. placed | 1 | No metal content |
| Second group of metallic plates | 10 × 10 (5 ×5 each) | 14 | 3 plates |
| Metallic can (cylindrical) | 12 ∅, 14 long | 18 | Can lids perpendicular to air-ground interface |
| Two stacked plastic disks | 18 ∅, 2 thickness | 2 | |
| Metallic disk | 18 ∅ | 9 | |
| 7.5 litre plastic jug (empty) | 29 long × 22 width × 12 thick | 1 | |
| TS-50 anti-personnel landmine [29] | 9 ∅ 4.5 thickness | 1 | Minimum metal content |
| VS-1.6 anti-tank landmine [30] | 22 ∅ 9.2 thickness | 5 | No metal content |
| Third group of metallic plates | 10 × 10 (5 ×5 each) | 8 | 3 plates |



**FIGURE 9.** Pictures of the UAV prototype conducting the scanning of the first validation scenario. Prototype fitted with (a) *large Vivaldi* antennas, (b) *customized Vivaldi* antennas, and (c) *small Vivaldi* antennas.

resulting GPR-SAR images exhibited a dispersive response, that is, echoes corresponding to the targets were not focused in range or depth, sometimes appearing several echoes (at different depths) for a single target. That makes the analysis and identification of buried targets very difficult. Therefore, due to their poor performance in terms of GPR-SAR imaging, *dual-polarized Vivaldi* antennas have not been included in the comparison conducted in this Section.

The positioning and geo-referencing subsystem is composed by a GNSS-RTK module [27] and a laser rangefinder [28] for accurate measurement of the height above ground. A detailed description of the implemented airborne-based GPR prototype can be found in [12]. Flights were performed at a height of 1.5 m above ground (see Fig. 9). This average height is considered a good trade-off between free-space attenuation losses and flight stability and safety (given the size of the UAV, the ground effect is noticeable when flying closer to the ground).

The objects listed in Table 2 and shown in Fig. 10 were buried to test the detection capabilities as a function of the antenna integrated in the UAV. Different types of targets were considered, both metallic and non-metallic, with different geometries and buried depths.

The 1.5 m width scanning domain was discretized into 31 along-track sweeps (spacing between two consecutive
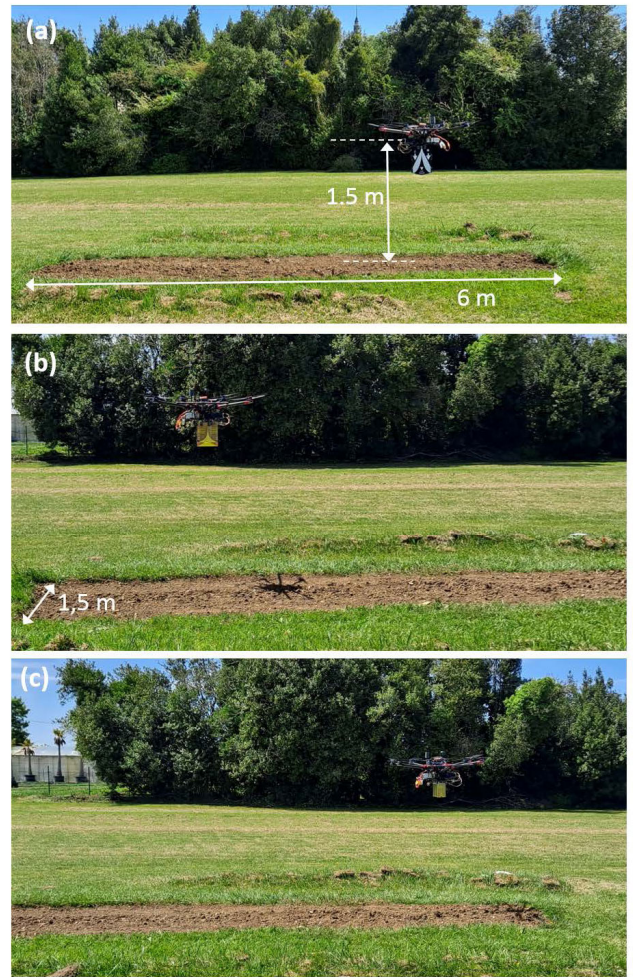
sweeps of 5 cm). Along-track scans were performed at a speed of 75 cm/s.

Fig. 11 shows a comparison of the flight paths performed by the UAV during the scan with each set of antennas. It must be remarked that wind gusts up to 25 km/h were experienced during the time the flights were conducted, resulting in the differences between flight paths depicted in Fig. 11. Nevertheless, these differences are small enough not to have an influence on the comparison of the 3D GPR-SAR reflectivity images associated with each antenna.

GPR measurements obtained with each set of antennas were processed following the same steps according to the workflow indicated in Section II.B of [12]. Singular Value Decomposition (SVD) filtering (Section III of [12]) was also applied finding that, on average, better detection results were achieved with the removal of the two first singular values, which correspond mainly to the air-soil clutter contribution. 3D GPR-SAR reflectivity was recovered in a volume of 5.6 m length × 1.5 m width × 0.8 m depth (20 cm above ground,

**FIGURE 10.** Picture of the targets buried in the scanned scenario.



**FIGURE 11.** Comparison of the flight paths followed by the UAV in the first validation scenario, when placed onboard (a) *large Vivaldi* antennas, (b) *customized Vivaldi* antennas, and (c) *small Vivaldi antennas*. Dots represent the geo-referred positions where measurements were taken. Blue dots: all the positions within x = [−0.75 0.75] m and y = [0.4 6] m. Red dots: selected measurement positions for GPR-SAR processing according to [12].

60 cm below ground, being z = 0 m the average position of the air-soil interface).

XY cuts of the recovered 3D GPR-SAR reflectivity are depicted in Fig. 12, where each row corresponds to the results of each kind of antenna. Columns correspond to cuts with similar depth. It must be pointed out that free-space back-propagation was considered in the GPR-SAR processing, so targets are detected deeper than their true depth. In particular, to calculate the true depth of the cuts, $z_{\text{true}} = z_{\text{GPR-SAR}}/\sqrt{\varepsilon_r}$ (for example, for the cut $z = -14$ cm, the true depth would be between 5.3 - 5.7 cm if we consider $\varepsilon_r$ ranging from 6 to 7).

Automatic target detection is performed by means of a 2D-cell-averaging constant false alarm rate (CFAR) algorithm. This algorithm is applied on each horizontal (XY) plane of the 3D GPR-SAR reflectivity images [8]. In the results depicted in Sections III.A and III.B, a radial distance of 35 cm from the true location of the target is considered to determine if the CFAR detection corresponds to a true
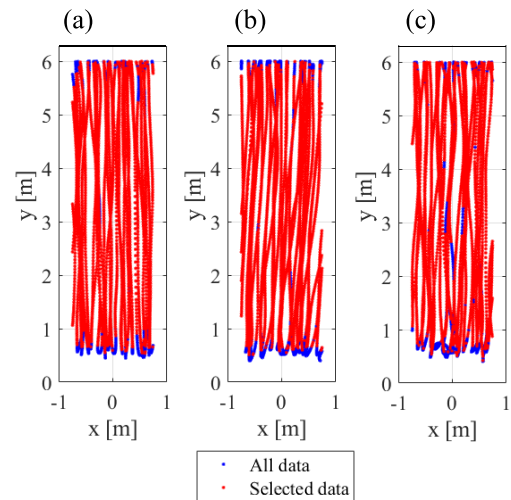
detection (depicted in green color in GPR-SAR images) or to a false positive (depicted in red color).

The two groups of metallic plates buried 14 cm deep are detected in all the cases (fourth column of Fig. 12, z = −34 cm, corresponding to a true depth of 12.9 cm − 13.9 cm), as well as the third group of metallic plates. The two stacked plastic disks and the metallic disk are also detected with the three sets of antennas (first two columns of Fig. 12). In the case of the 7.5 litre plastic jug, the reflection happening at the bottom side of the jug (interface between the air inside the jug and the soil below the jug) is detected at around z = −26 cm when using the *large Vivaldi* antennas, while the upper reflection is detected with the *small and customized Vivaldi* antennas. Concerning the wooden-like IED, the CFAR algorithm detects it with the *large and customized Vivaldi* antennas. However, if the XZ cuts of the 3D GPR-SAR reflectivity are depicted (Fig. 13), the wooden-like IED is noticeable with the *small Vivaldi* antenna as well. Furthermore, in this XZ cut, the reflectivity of the IED top face has a strong level and two deeper reflections, which could correspond to the bottom face of the IED, can be noticed. Finally, although a reflection corresponding to the bottom face of the anti-tank landmine is detected by the CFAR algorithm only with the *small Vivaldi* antenna, this target can be also observed with the *large Vivaldi* antennas if the XZ cuts are plotted (Fig. 14).

The rest of the targets (the shallow anti-personnel landmine and the deeply buried metallic can) cannot be clearly identified, as the corresponding echoes located at the position of these targets have the same level as the clutter observed in the GPR-SAR reflectivity images. Only the anti-personnel landmine is detected by the CFAR algorithm with the *small*
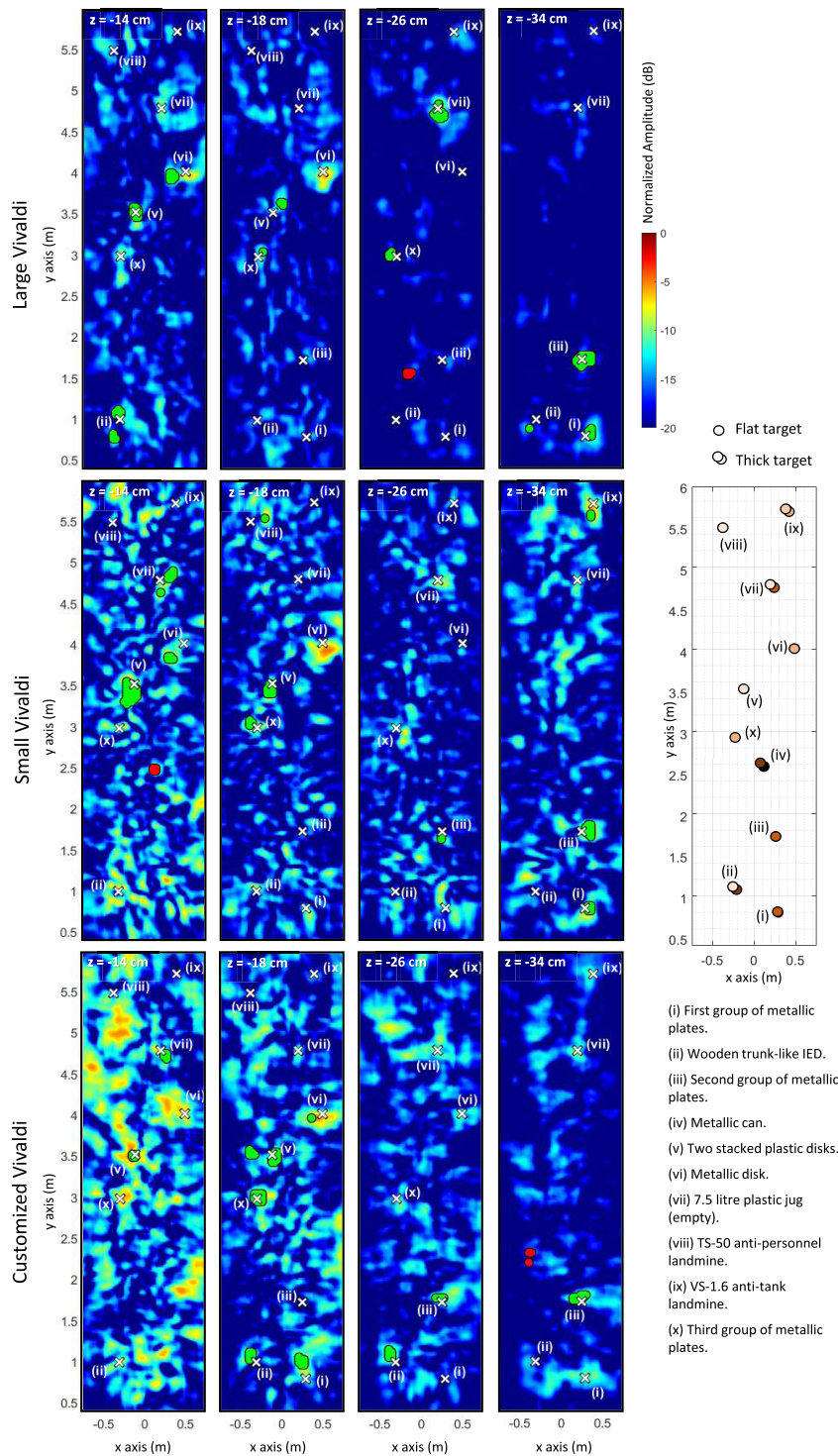
**FIGURE 12.** XY planes of the 3D GPR-SAR reflectivity (normalized, in dB) corresponding to the first validation scenario. Cuts centered at the depth where targets were detected. For the sake of clarity, only those XY cuts corresponding to clear detections are shown. Upper row corresponds to the detection results using the *large Vivaldi* antennas, middle row corresponds to the results using the *small Vivaldis*, and lower row corresponds to the *customized Vivaldis*. The true location of the targets is depicted with white crosses on the GPR-SAR images. In the scheme displayed on the right side of the figure, circles denoting the position of the targets are colored according to their true depth. CFAR detections are colored in red and green, depending on whether they correspond to a false alarm or a true detection, respectively. In the case of thick targets, color gives an idea of the depth of the upper and lower interfaces or boundaries of the target.
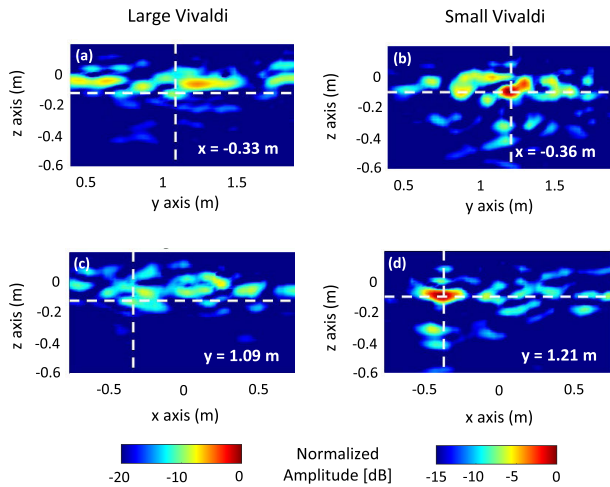
**FIGURE 13.** YZ and XZ planes of the 3D GPR-SAR reflectivity (normalized, in dB) centered at the position where the wooden trunk-like IED is detected with the *large Vivaldi* (YZ cut (a), and XZ cut (c)) and with the *small Vivaldi* (YZ cut (b) and XZ cut (d)).
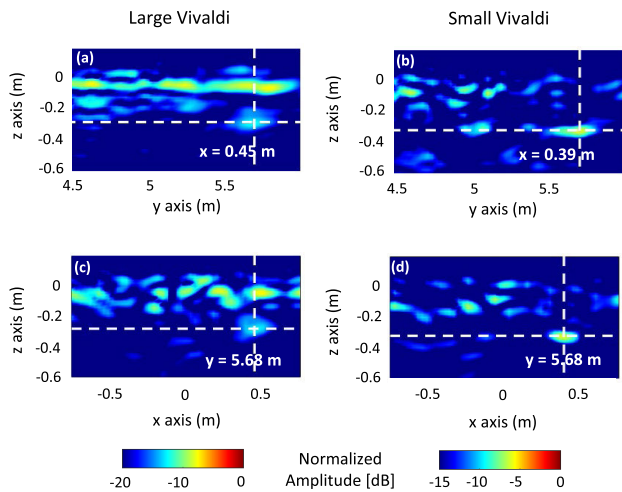


**FIGURE 14.** YZ and XZ planes of the 3D GPR-SAR reflectivity (normalized, in dB) centered at the position where the anti-tank landmine is detected with the *large Vivaldi* (YZ cut (a), and XZ cut (c)) and with the *small Vivaldi* (YZ cut (b) and XZ cut (d)).

*Vivaldi* antenna. Concerning signal-to-clutter ratio, results corresponding to *customized Vivaldi* antennas (third row) seem to exhibit slightly higher clutter levels at depths close to the soil surface, whereas those of the *small Vivaldi* (second row) seem to have higher clutter levels across all depths than the *large Vivaldi* antenna.

### B. SECOND VALIDATION SCENARIO

Within the framework of a measurement campaign in a realistic scenario to test the prototype presented in [12] in quasi-operational conditions, it was decided to compare the performance of the *large and small Vivaldi* antennas again, aiming to further improve the airborne-based GPR system. The validation scenario was the Spanish military training and

**TABLE 3.** Second validation scenario. Buried targets.

| Object | Size (cm) | Depth (cm) | Other specs. |
|---|---|---|---|
| Plastic bag filled with paper | 30 ⌀ aprox. | 5 | |
| Wooden pressure plate | 25 long × 7 width | 4 | |
| Wooden box filled with plasterboard | 30 long × 25 width × 20 thick | 5 | |
| VS-1.6 anti-tank landmine [30] | 22 ⌀ 9.2 thickness | 4 | No metal content |
| Two 81 mm mortar shells, metallic | 39 long × 8.1 ⌀ | 8 | |

shooting range "El Palancar", located north of Madrid. In this scenario, the soil is significantly drier than in the previous case (airfield of the University of Oviedo), estimating a relative permittivity around $\varepsilon_r = 4$ (a metallic plate buried 13 cm deep was used to obtain this estimation).

The scanned area, whose size was 4.5 m across-track by 12 m along-track, is shown in Fig. 15 and Fig. 16. Due to the size of the scanned area and the limited capacity of the UAV batteries, the scan was divided into three flights. These three flights took 30 minutes for each tested antenna. The 4.5 m across-track × 12 m along-track acquisition domain was discretized into 91 along-track sweeps, being the spacing between two consecutive sweeps of 5 cm. In this scenario, the average flight height was set to 1.2 m for the *large Vivaldi* and 1 m for the *small* ones, so that the distance from the soil surface to the antennas was almost the same in both cases. The same GPR measurement acquisition and processing methodology as in the first validation scenario were followed.

Flights were conducted with two different UAV platforms: the *large Vivaldi* antennas were mounted in the same UAV platform used in the first validation scenario [15] (Fig. 16), whereas the *small Vivaldi* antennas were mounted in a similar UAV platform [31], which has slightly less payload capacity. Nevertheless, except from the airframe model and the GPR antennas, the architecture and the subsystems mounted on board both prototypes were exactly the same.

IEDs and landmines were buried by personnel of the Counter Improvised Explosive Devices Center of Excellence (C-IED CoE) [32] and from the Ministry of Defense of Spain resembling the conditions and placement of real scenarios. The targets listed in Table 3 will be considered to compare the antennas. Since these targets were buried in an area ranging from y = 0 m to y = 7.3 m (along-track axis), the 3D GPR-SAR reflectivity images will be limited to that along-track interval. As in the first validation scenario, 2D CFAR processing was applied to the XY cuts of the 3D GPR-SAR reflectivity images for automatic detection of potential buried targets.

Cuts of the 3D GPR-SAR reflectivity are shown in Fig.17 for the case of the *large Vivaldi*, and in Fig. 18 for the *small*
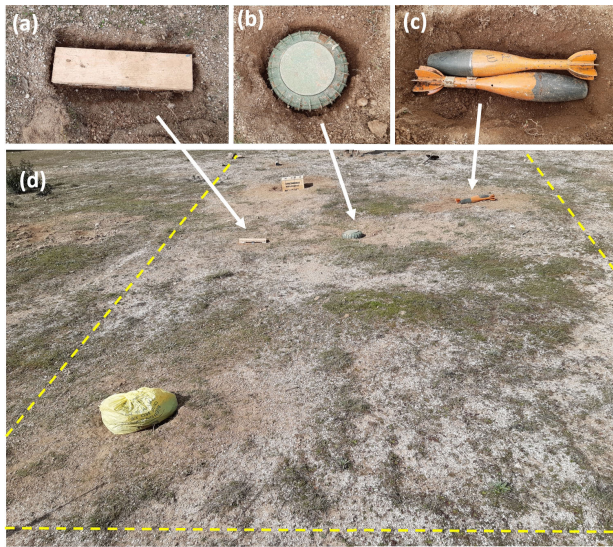
**FIGURE 15.** Overview of the second scenario and buried targets. (a) Wooden pressure plate. (b) VS-1.6 anti-tank plastic landmine [30]. (c) Metallic mortar shells. (d) Picture of the scanned area showing the targets (uncovered) at the positions where they were buried. The plastic bag filled with paper can be seen in the lower left side of the picture, and the wooden box filled with plasterboard, on the top center of the picture (between the wooden pressure plate and the VS-16 anti-tank landmine).

*Vivaldis*. In both cases, the targets that are better detected are the wooden box and the filled plastic bag. It is worth noting that both the upper and lower part of the wooden box are clearly detected, especially in the results corresponding to the *large Vivaldi* antennas. Therefore, an estimate of the permittivity of the plasterboard can be given from the knowledge of the distance between the upper and lower echoes observed in the vertical cut of the reflectivity ($z_{top} = -12$ cm, $z_{bottom} = -44$ cm), so $\varepsilon_{r,plasterboard} \approx (30 \text{ cm} / 20 \text{ cm})^2 = 2.6$. Concerning the remaining targets, the two 81 mm mortar shells and the anti-tank mine are found at $z = -24$ cm (which

corresponds to a true depth of 12 cm approximately) with both antennas. However, the wooden pressure plate cannot be detected with the *small Vivaldis*.

The plastic bag filled with paper has a noticeable reflectivity response (Fig. 17, and Fig. 18, target (1)), which can be due to its low permittivity (the relative permittivity of paper is around $\varepsilon_r = 2.3$), with respect to the surrounding medium (soil, $\varepsilon_r = 4$).

## IV. DISCUSSION

Detection results for the first and second scenarios are summarized in Table 4. In the case of the first scenario, the *customized Vivaldi* antennas yield the worst detection capabilities (although they might be slightly better for detecting deep targets, since they provided good results for the metallic plates). Some targets are better detected with the *small Vivaldis* (e.g. the wooden trunk-like IED), whereas others (e.g. the 7.5 litre plastic jug) can be better distinguished with the *large Vivaldi*. However, it is worth noting that the results of the former (*small Vivaldis*) exhibit higher levels of clutter. Results for the second scenario show better performance of the *large Vivaldi* antennas with respect to the *small* ones in terms of detection capabilities and signal-to-clutter ratio.

As expected, clutter coming from the air-soil reflection partially masks shallow targets. Among these shallow targets, those having a significant thickness (e.g. the wooden box, the plastic jug, the wooden trunk-like IED, or the anti-tank landmine) can be detected as the reflection between the bottom of the target and the soil occurs deep enough so that it is not masked by the air-soil clutter.

In terms of penetration depth capabilities, the three compared antennas seem to have similar performance: the two sets of metallic plates buried 14 cm deep and the one buried 8 cm deep are detected in all the cases.

The shape of the buried targets also has an impact in the detectability. For example, in the first scenario, the metallic can is buried only 4 cm deeper than the two sets of metallic



**FIGURE 16.** Picture of UAV prototype scanning the scenario when fitted with the large Vivaldi antennas.
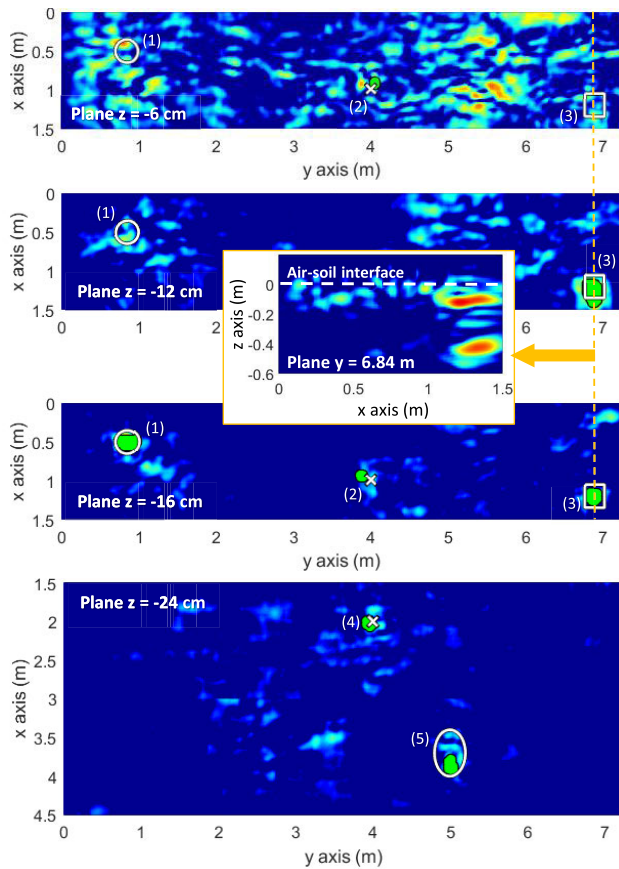
**FIGURE 17.** XY planes of the 3D GPR-SAR reflectivity (normalized, in dB) corresponding to the second validation scenario and the *large Vivaldi* antennas. Cuts centered at the depth where targets were detected. For the sake of clarity, only those XY cuts corresponding to clear detections are shown. CFAR detections are colored in red and green, depending on whether they correspond to a false alarm or a true detection, respectively. Buried targets: (1) plastic bag filled with paper, (2) wooden pressure plate, (3) wooden box filled with plasterboard, (4) VS-1.6 anti-tank landmine, (5) two 81 mm mortar shells. For the largest targets, the white solid line provides an estimate of their size. The vertical (XZ) cut centered at the location of the wooden box (3) is also shown.



**FIGURE 18.** XY planes of the 3D GPR-SAR reflectivity (normalized, in dB) corresponding to the second validation scenario and the *small Vivaldi* antennas. Cuts centered at the depth where targets were detected. For the sake of clarity, only those XY cuts corresponding to clear detections are shown. CFAR detections are colored in red and green, depending on whether they correspond to a false alarm or a true detection, respectively. Buried targets: (1) plastic bag filled with paper, (2) wooden pressure plate, (3) wooden box filled with plasterboard, (4) VS-1.6 anti-tank landmine, (5) two 81 mm mortar shells. For the largest targets, the white solid line provides an estimate of their size. The vertical (XZ) cut centered at the location of the wooden box (3) is also shown.

plates buried 14 cm deep and it is even larger than those ones. However, it is not detected in any case. The main reason is that this cylindrical-shaped can is buried lying on its side, resulting in little reflection. A similar effect is observed in the second scenario, where the two metallic mortar shells exhibit lower reflectivity than the smaller plastic VS-1.6 anti-tank landmine. The latter has flat top and bottom sides, resulting in stronger reflection than the smooth, rounded shapes of the metallic mortar shells.

Putting together the detection results with the radiation performance of the compared Vivaldi antennas, several conclusions can be extracted:

- The *small Vivaldi* antenna has a large variation of the phase center (Fig. 8), which might be related to the fact that the GPR-SAR images exhibit higher levels of clutter.
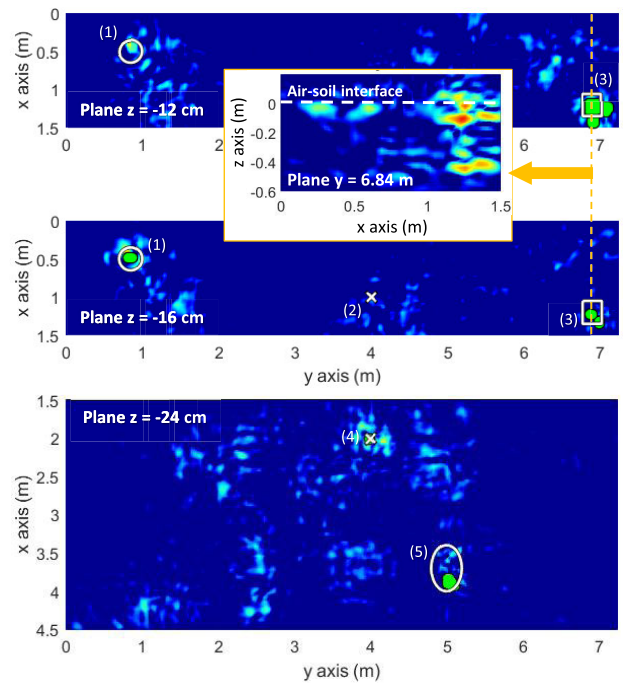
- *Small and large Vivaldis* show a smooth variation of the boresight level (Fig. 7) and the directivity (Fig. 5), which is more irregular in the case of the *customized Vivaldis*. Even though equalization of the frequency response is applied in the GPR-SAR processing, this could be one of the factors explaining the worse detectability achieved with the *customized Vivaldi* antennas.

Concerning the selection of the antennas for the airborne-based GPR system, it is concluded that, although *large Vivaldi* antennas are a bit bulky (making the flights more difficult, especially under windy conditions), they exhibit the best performance in terms of detection capabilities. This is in agreement with the fact that their electrical size allows achieving the best radiation performance (highest directivity) of the compared antennas. Nevertheless, *small Vivaldi* antennas could be considered a potential candidate in case of more restrictive size and weight requirements for the UAV integration.

Another criterion for the selection of the UWB antennas could be the cost. In this sense, *small and large Vivaldi* antennas are around 3 times cheaper than the *dual-polarized Vivaldis*, and up to 6 times cheaper than some models of spiral

**TABLE 4.** Detection results, both scenarios. Quantitative detection analysis based on CFAR processing of the 3D GPR-SAR images shown in Fig. 12 - Fig. 14 for the first validation scenario, and in Fig. 17 and Fig. 18 for the second validation scenario. Intervals in dB given for each target correspond to the reflectivity level of the detected target with respect to the clutter observed in the corresponding cut in the GPR-SAR images.

| Object | *Large Vivaldi* [17] | *Small Vivaldi* [19] | *Customized Vivaldi* |
|---|---|---|---|
| SCENARIO 1 | | | |
| First group of metallic plates | Detected 5-10 dB | Detected 10-15 dB | Detected 10-15 dB |
| Wooden trunk-like IED | Detected 0-5 dB | Detected* 10-15 dB | Detected 0-5 dB |
| Second group of metallic plates | Detected 5-10 dB | Detected 5-10 dB | Detected 5-10 dB |
| Metallic can | Not detected | Not detected | Not detected |
| Two stacked plastic disks | Detected 10-15 dB | Detected 15-20 dB | Detected 0-5 dB |
| Metallic disk | Detected 10-15 dB | Detected 10-15 dB | Detected 5-10 dB |
| 7.5 litre plastic jug (empty) | Detected 5-10 dB | Detected 0-5 dB | Detected 0-5 dB |
| TS-50 anti-personnel landmine [29] | Not detected | Detected 0-5 dB | Not detected |
| VS-1.6 anti-tank landmine [30] | Detected* 0-5 dB | Detected 5-10 dB | Not detected |
| Third group of metallic plates | Detected 5-10 dB | Detected 5-10 dB | Detected 5-10 dB |
| SCENARIO 2 | | | |
| (1) Plastic bag filled with paper | Detected 10-15 dB | Detected 5-10 dB | N/A |
| (2) Wooden pressure plate | Detected 5-10 dB | Not detected | N/A |
| (3) Wooden box with plasterboard | Detected 15-20 dB | Detected 15-20 dB | N/A |
| (4) VS-1.6 anti-tank landmine [30] | Detected 10-15 dB | Detected 5-10 dB | N/A |
| (5) Two 81 mm mortar shells | Detected 5-10 dB | Detected 0-5 dB | N/A |

* denotes a target not detected by the CFAR processing that, however, can be identified from a visual inspection of GPR-SAR images.

antennas. Still, the cost of the UWB antennas is not a critical limitation, as they are much cheaper than the overall cost of the rest of the hardware of most of the UAV-based GPR systems.

## V. CONCLUSION
A comparison of different Vivaldi antennas for an airborne-based GPR system has been presented in this contribution.

This comparison comprises the antenna characterization from measurements at spherical range in anechoic chamber, as well as testing the antennas onboard a UAV in realistic scenarios for landmine and IED detection.

Results obtained in this contribution are in line with the kind of antennas proposed in [8], [10], where directive and low-dispersive antennas were considered for these airborne-based GPR systems. The main advantages of the Vivaldi antennas [17] considered in this contribution are: i) they are commercial, low-cost antennas, ii) they occupy less volume than the Vivaldi-horn antennas proposed in [8], [10] and iii) they provide good detection capabilities. Besides, it has been proved that smaller Vivaldi antennas are also a feasible solution even though the detection capabilities are slightly worsened.

From the GPR-SAR results it was found that, in the case of large buried targets, an estimate of the permittivity of the target can be extracted, and thus, its composition. This could be of special interest to obtain a first guess of the kind of explosive within a non-metallic IED.

### REFERENCES
[1] I. J. Won, D. A. Keiswetter, and T. H. Bell, "Electromagnetic induction spectroscopy for clearing landmines," *IEEE Trans. Geosci. Remote Sens.*, vol. 39, no. 4, pp. 703–709, Apr. 2001.

[2] M. Sato, X. Feng, and J. Fujiwara, "Handheld GPR and MD sensor for landmine detection," in *Proc. IEEE Antennas Propag. Soc. Int. Symp.*, Jul. 2005, pp. 1–4.

[3] P. G. de Santos, E. Garcia, J. Estremera, and M. A. Armada, "DYLEMA: Using walking robots for landmine detection and location," *Int. J. Syst. Sci.*, vol. 36, no. 9, pp. 545–558, Jul. 2005.

[4] A. Ismail, M. Elmogy, and H. ElBakry, "Landmines detection using autonomous robots: A survey," *Int. J. Emerg. Trends Technol. Comput. Sci.*, vol. 3, no. 4, pp. 183–187, 2014.

[5] M. Peichl, E. Schreiber, A. Heinzel, and T. Kempf, "TIRAMI-SAR—A synthetic aperture radar approach for efficient detection of landmines and UXO," in *Proc. 10th Eur. Conf. Synth. Aperture Radar (EUSAR)*, 2014, pp. 1–4.

[6] (May 2021). *Mine Kafon Project*. [Online]. Available: http://minekafon.org/

[7] L.-S. Yoo, J.-H. Lee, S.-H. Ko, S.-K. Jung, S.-H. Lee, and Y.-K. Lee, "A drone fitted with a magnetometer detects landmines," *IEEE Geosci. Remote Sens. Lett.*, vol. 17, no. 12, pp. 2035–2039, Dec. 2020.

[8] M. Schartel, R. Burr, R. Bähnemann, W. Mayer, and C. Waldschmidt, "An experimental study on airborne landmine detection using a circular synthetic aperture radar," 2020, *arXiv:2005.02600*. [Online]. Available: http://arxiv.org/abs/2005.02600

[9] J. Colorado, M. Perez, I. Mondragon, D. Mendez, C. Parra, C. Devia, J. Martinez-Moritz, and L. Neira, "An integrated aerial system for landmine detection: SDR-based ground penetrating radar onboard an autonomous drone," *Adv. Robot.*, vol. 31, no. 15, pp. 791–808, 2017.

[10] D. Šipoš and D. Gleich, "A lightweight and low-power UAV-borne ground penetrating radar design for landmine detection," *Sensors*, vol. 20, no. 8, p. 2234, Apr. 2020.

[11] E. Schreiber, A. Heinzel, M. Peichl, M. Engel, and W. Wiesbeck, "Advanced buried object detection by multichannel, UAV/drone carried synthetic aperture radar," in *Proc. 13th Eur. Conf. Antennas Propag. (EuCAP)*, 2019, pp. 1–5.

[12] M. Garcia-Fernandez, Y. A. Lopez, and F. L.-H. Andres, "Airborne multi-channel ground penetrating radar for improvised explosive devices and landmine detection," *IEEE Access*, vol. 8, pp. 165927–165943, 2020.

[13] R. Kazemi, "Development of a logarithmic spiral antenna in UWB GPR for humanitarian demining," *Electromagnetics*, vol. 38, no. 6, pp. 366–379, Aug. 2018.

[14] D. A. Crocker and W. R. Scott, "An unbalanced sinuous antenna for near-surface polarimetric ground-penetrating radar," *IEEE Open J. Antennas Propag.*, vol. 1, pp. 435–447, 2020.

[15] (May 2021). *Spreading Windows S1000+ From DJI*. [Online]. Available: https://www.dji.com/spreading-wings-s1000-plus

[16] (May 2021). *M:Explore UWB Radar From ILMSens*. [Online]. Available: https://www.ilmsens.com/products/m-explore/

[17] (May 2021). *TSA600 Vivaldi Antenna From RFSpace*. [Online]. Available: http://rfspace.com/RFSPACE/Antennas_files/TSA600.pdf

[18] (May 2021). *TC-93083A UWB Antenna From TESCOM*. [Online]. Available: http://en.tescom.co.kr/product/product4?code=040204/

[19] (May 2021). UWB Antenna IS-AV-0106G From ILMSens. [Online]. Available: https://www.ilmsens.com/products/

[20] (May 2021). LPKF Protomat H100 From LPKF. [Online]. Available: https://www.lpkfusa.com/datasheets/prototyping/h100.pdf

[21] W.-H. Tu and K. Chang, "Wide-band microstrip-to-coplanar stripline/slotline transitions," *IEEE Trans. Microw. Theory Techn.*, vol. 54, no. 3, pp. 1084–1089, Mar. 2006.

[22] Z. Hu, Z. Zeng, K. Wang, W. Feng, J. Zhang, Q. Lu, and X. Kang, "Design and analysis of a UWB MIMO radar system with miniaturized Vivaldi antenna for through-wall imaging," *Remote Sens.*, vol. 11, no. 16, p. 1867, Aug. 2019. [Online]. Available: https://www.mdpi.com/2072-4292/11/16/1867

[23] M. Abbak, M. N. Akinci, M. Çayören, and I. Akduman, "Experimental microwave imaging with a novel corrugated Vivaldi antenna," *IEEE Trans. Antennas Propag.*, vol. 65, no. 6, pp. 3302–3307, Jun. 2017.

[24] M. Gonzalez-Diaz, M. Garcia-Fernandez, Y. Alvarez-Lopez, and F. Las-Heras, "Improvement of GPR SAR-based techniques for accurate detection and imaging of buried objects," *IEEE Trans. Instrum. Meas.*, vol. 69, no. 6, pp. 3126–3138, Jun. 2020.

[25] Y. Yang, B.-Z. Wang, and S. Ding, "Performance comparison with different antenna properties in time reversal ultra-wideband communications for sensor system applications," *Sensors*, vol. 18, no. 1, p. 88, Dec. 2017.

[26] P. Padilla, P. Pousi, A. Tamminen, J. Mallat, J. Ala-Laurinaho, M. Sierra-Castaner, and A. V. Raisanen, "Experimental determination of DRW antenna phase center at mm-wavelengths using a planar scanner: Comparison of different methods," *IEEE Trans. Antennas Propag.*, vol. 59, no. 8, pp. 2806–2812, Aug. 2011.

[27] (May 2020). *GNSS-RTK From Topcon*. [Online]. Available: https://www.topconpositioning.com/oem-components-technology/

[28] (May 2020). *LIDAR Altimeter From Lightware Optoelectronics*. [Online]. Available: https://lightwarelidar.com/collections/lidar-rangefinders/products/sf11-b-50-m

[29] (May 2020). *TS-50 Anti-Personnel Landmine*. [Online]. Available: https://en.wikipedia.org/wiki/TS-50_mine

[30] (May 2020). *VS-1.6 Anti-Tank Landmine*. [Online]. Available: https://en.wikipedia.org/wiki/VS-1.6_mine

[31] (May 2020). *X8 From Tarot*. [Online]. Available: http://www.helipal.com/tarot-x8-octocopter-frame-set.html

[32] (May 2020). *Counter Improvised Explosive Devices Center of Excellence (C-IED CoE)*. [Online]. Available: https://www.ciedcoe.org/

**MARÍA GARCÍA FERNÁNDEZ** was born in Luarca, Spain, in 1992. She received the M.Sc. and Ph.D. degrees in telecommunication engineering from the University of Oviedo, Spain, in 2016 and 2019, respectively. Since 2013, she has been involved in several research projects with the Signal Theory and Communications Research Group, TSC-UNIOVI, University of Oviedo. She was a Visiting Student with Stanford University, Palo Alto, CA, USA, from 2013 to 2014; a Visiting Scholar with the Gordon Center for Subsurface Sensing and Imaging Systems, Northeastern University, Boston, MA, USA, in 2018; and a Visiting Researcher at the Radar Department, TNO, The Hague, The Netherlands, in 2019. Her current research interests include inverse scattering, remote sensing, radar systems, imaging techniques, antenna measurement and diagnostics, and non-invasive measurement systems on board unmanned aerial vehicles. She was a recipient of the 2020 National Award to the Best Ph.D. Thesis on Telecommunication Engineering (category: telecommunications technologies and applications).

**GUILLERMO ÁLVAREZ NARCIANDI** received the M.Sc. degree in telecommunication engineering and the Ph.D. degree from the University of Oviedo, Gijón, Spain, in 2016 and 2020, respectively. He was a Visiting Student with Stanford University, CA, USA, in 2014; a Visiting Scholar with the University of Pisa, Italy, in 2018; and with the Institute of Electronics, Microelectronics and Nanotechnology (IEMN), University of Lille, France, in 2019. His research interests include radar systems and imaging techniques, antenna diagnosis and characterization systems, localization and attitude estimation systems, and RFID technology. He received the AMTA 2019 Student Paper Award (second place) and the Special Award to the Best Entrepreneurship Initiative in XV Arquímedes National Contest, in 2017, for the development of a RFID-based location system.

**ANA ARBOLEYA** (Member, IEEE) received the M.Sc. and Ph.D. degrees in telecommunication engineering from the University of Oviedo, Spain, in 2009 and 2016, respectively. From 2008 to 2016, she worked as a Research Assistant with the Signal Theory and Communications Research Group, Department of Electrical Engineering, TSC-UNIOVI, University of Oviedo. From 2014 to 2015, she was a Visiting Scholar with the MilliLab, Department of Radio Science and Engineering, Aalto University, Finland. In 2017, she held a postdoctoral position at the EpOC Polytech' Laboratory (electronics for connected objects), University of Nice-Sophia Antipolis, France. She is currently an Associate Professor with Universidad Rey Juan Carlos, Madrid, Spain. Her major research interests include antenna diagnostics and measurement systems and techniques and high frequency imaging techniques and applications. She was a recipient of the 2017 National Awards of the Official College of Telecommunication Engineers of Spain to the Best Ph.D. Thesis on Telecommunication.

**CARLOS VÁZQUEZ ANTUÑA** received the M.Sc. degree in telecommunication engineering, the M.Sc. degree in information technology and mobile communications, and the Ph.D. degree from the University of Oviedo, Gijón, Spain, in 2007, 2008, and 2013, respectively. From 2007 to 2012, he was a Graduate Research Assistant with the Signal Theory and Communications Group, University of Oviedo, where he has been a Research Fellow, since 2012. His current research interests include nonlinear analysis and optimization techniques for the design of multifunctional oscillator-based circuits, active antennas, and passive components, such as frequency multipliers and harmonic mixers, at microwave, millimeter/submillimeter-wave, and terahertz frequencies.

**FERNANDO LAS-HERAS ANDRÉS** (Senior Member, IEEE) received the M.S. and Ph.D. degrees in telecommunication engineering from the Technical University of Madrid (UPM), in 1987 and 1990, respectively. He was a National Graduate Research Fellow (1988–1990) and he held a position of an Associate Professor at the Department of Signal, Systems and Radiocommunications, UPM, from 1991 to 2000. He has been heading the research group Signal Theory and Communications, TSC-UNIOVI, Department of Electrical Engineering, University of Oviedo, since 2001. Since December 2003, he has been a Full Professor with the University of Oviedo, where he was the Vice Dean for telecommunication engineering at the Technical School of Engineering (2004–2008). He was a Visiting Lecturer at the National University of Engineering in Peru, in 1996; a Visiting Researcher at Syracuse University, NY, USA, in 2000; and a short-term Visiting Lecturer at ESIGELEC, France, from 2005 to 2011. He held the Telefónica Chair on ''RF Technologies,'' ''ICTs applied to Environment,'' and ''ICTs and Smartcities'' at the University of Oviedo (2005–2015). He has led and participated in a great number of research projects and has authored over 220 articles published in indexed scientific journals on topics of antennas, propagation, metamaterials and inverse problems with application to antenna measurement, electromagnetic imaging and localization, developing computational electromagnetics algorithms and technology on microwaves, millimeter wave, and THz frequency bands. He was a member of the Board of Director of the IEEE Spain Section (2012–2015), a member (2016–2017) and the Vice-President (2020–2022) of the Board of the Joint IEEE MTT-S and AP-S Spain Chapter, a member of the Science, Technology and Innovation Council of Asturias (2010–2012), and the President of the Professional Association of Telecommunication Engineers, Asturias.

**YURI ÁLVAREZ LÓPEZ** received the M.S. and Ph.D. degrees in telecommunication engineering from the University of Oviedo, Spain, in 2006 and 2009, respectively. He was a Visiting Scholar at the Department of Electrical Engineering and Computer Science, Syracuse University, Syracuse, USA, in 2008; a Visiting Postdoctoral Researcher at the Gordon Center for Subsurface Sensing and Imaging Systems (CenSSIS) ALERT Center of Excellence, Northeastern University, Boston, USA, from 2011 to 2014; and a Visiting Postdoctoral Researcher at ELEDIA Research Center, Trento, Italy, in 2015. He has been with the Signal Theory and Communications Research Group, University of Oviedo, Gijón, Spain, since 2006, where he is currently a Professor. His research interests include antenna diagnostics, antenna measurement techniques, RF techniques for indoor location, inverse scattering and imaging techniques, and phaseless methods for antenna diagnostics and imaging. He was a recipient of the 2011 Regional and National Awards to the Best Ph.D. Thesis on Telecommunication Engineering (category: security and defense).

• • •